# Understanding variant selection and texture in additively manufactured red-gold alloys

Hossein Ghasemi-Tabasi [a],[*], Margaux N.D. Larcher [a], Cyril Cayron [a], Jamasp Jhabvala [a], Steven Van Petegem [b], Nikola Kalentics [a], Eric Boillat [a], Roland E. Logé [a]

[a] Thermomechanical Metallurgy Laboratory (LMTM)-PX Group Chair, École Polytechnique Fédérale de Lausanne (EPFL), Neuchâtel CH-2002, Switzerland
[b] Photons for Engineering and Manufacturing, Paul Scherrer Institute, Forschungsstrasse 111, Villigen 5232, Switzerland

## ARTICLE INFO

## ABSTRACT

Printing gold alloys parts is a challenge due to the high reflectivity and thermal conductivity of these materials. Recent studies show an improvement in printing gold using the Laser Powder Bed Fusion (L-PBF) process; however, the impact of the $A1 \rightarrow L1_0$ phase transformation on printed red-gold alloy has not been studied. In this work, 3D printed red-gold samples with different post-processing conditions have been heat-treated at 250 °C to investigate the effect of the sample stress states on variant selection, by Electron Backscatter Diffraction. Synchrotron X-ray diffraction experiments reveal the presence of a non-negligible amount of tetragonal phase in the as-build red-gold samples. The use of an intermediate heat treatment at 600 °C to eliminate small domains of tetragonal phase formed during the manufacturing process demonstrates that the crystallographic textures following heat treatment are highly dependent on the stress-state during the early stage of the phase transformation.

Among different additive manufacturing (AM) techniques, the Laser Powder Bed Fusion (L-PBF) has received the most focus. A result of the deposition of liquid material on a solid substrate with lower temperature or previous solidified layers, is the existence of high temperature gradients and generation of residual stresses [1]. Spatial thermal gradients due to localized heating and cooling, and associated thermal expansion and contraction, including those coming from phase transformations (solid-liquid, or solid-solid), explain the generation of residual stresses in L-PBF. Restricted thermal shrinkage is the main reason for the presence of high tensile residual stresses in regions near the upper surface of the part under construction. After printing, tensile stresses on the top of the part are compensated by compressive stresses underneath, such as to satisfy stress equilibrium [2]. Laser Shock Peening (LSP) has recently been used in AM to transform the tensile residual stresses into compressive ones, in the near surface region [3–5], which permits to improve the mechanical properties of the piece [6].

Due to the high thermal gradients during the printing and the strong residual stresses remaining in the final piece, the processing is even more challenging when performed on a material undergoing a phase transformation. It is particularly the case for red-gold

alloys close to the equiatomic AuCu composition, undergoing an order-disorder phase transformation $A1 \rightarrow L1_0$ around 400 °C [7,27]. At high temperature, the stable phase is a disordered f.c.c. (face centered cubic) lattice A1 with the gold and copper atoms randomly distributed on the lattice sites. Under the transformation temperature, the stable phase is a f.c.t. (face centered tetragonal) phase named AuCuI. This $L1_0$ superlattice results from the tetragonal distortion of the f.c.c. lattice associated with the ordering of the gold and copper atoms on alternate (002) planes. As local diffusion is needed for the atomic ordering, a high cooling rate can prevent the phase transformation, and the f.c.c. phase can be maintained in a metastable state at room temperature. However, the kinetics of the phase transformation highly depends on the temperature of the previous annealing treatment [8,28].

The f.c.t. phase can be obtained from retained f.c.c by a subsequent heat treatment under 400 °C often called hardening heat treatment. The f.c.t. phase is beneficial for the mechanical properties of the material and is often used in industry for increasing the hardness and yield stress [9,25] . However, the phase transformation is also known for inducing strong macroscopic distortion in the material, that can even lead to cracking [9–12]. In a recent study [13], we have shown that a red gold bar in cubic (f.c.c) state that is slightly bent elastically continues to bend during the cubic to tetragonal (f.c.t) transformation, even when stress is no longer

---

* Corresponding author.
*E-mail address:* hossein.ghasemitabasi@epfl.ch (H. Ghasemi-Tabasi).

**Table 1**
L-PBF process parameters and post treatments for bronze and red-gold samples.

|  | Power(W) | Speed(mm/s) | Hatching distance(µm) | Layer thickness(µm) | Laser beam diameter (µm) |
|---|---|---|---|---|---|
| Bronze | 200 | 275 | 100 | 40 | 65 |
| Red-gold | 320 | 200 | 100 | 40 | 65 |

**Table 2**
Different post processing treatments applied on as-built L-PBF red-gold samples. The treatments are applied sequentially from left to right, for each sample.

|  | Annealing at 600 °C for 1 h | LSP | Hardening heat treatment at 250 °C for 3 h |
|---|---|---|---|
| Sample 1 | × | × | ✓ |
| Sample 2 | × | ✓ | ✓ |
| Sample 3 | ✓ | ✓ | ✓ |

applied. This macroscopic distortion was shown to be initiated at the early stages of the transformation, even under small stress levels. This singular behavior was named Thermally Activated Distortion with Amplification (TADA) effect. It is explained as follows. First, the stress is released by classical stress-induced variant selection, and second, the amplification is caused by the persistence of the initial variant selection during the continuation of the phase transformation. This variant selection has been proved to persist during further heat treatment, even under opposite loading [14].

Due to the strong residual stresses in final printed parts, an important variant selection is expected during a hardening heat treatment on nearly 100% f.c.c. as-built pieces. In this study, we quantify residual stresses effects on the preferential crystallographic orientations of the grains (crystallographic texture) of 3D printed red-gold after hardening treatment. In particular, we show that surprisingly, the strong compressive stress induced by the LSP treatment after L-PBF printing has no impact on the final texture of the f.c.t. phase. This behavior is explained by the formation of small f.c.t. domains with tensile variant selection during printing, which persist despite the subsequent LSP induced compressive stress.

L-PBF experiments of bronze and red-gold samples were performed with an in-house machine developed for research activities [15] and designed for operating with only a few dozen grams of powder. The use of bronze samples in this study aims at measuring the residual stress in the as-built and LSP treated states, using the hole drilling method, assuming these are close to the ones obtained in red-gold (See Supplementary Section S1 for more information). Table 1 summarizes the process parameters used to print the samples.

The laser parameters optimization process via experiments and simulations can be found in [16–18]. Table 2 summarizes the post-processing treatments applied on 3 different red-gold samples.

While still being attached to the baseplate, some samples were treated with laser shock peening (LSP) using a Nd:YAG SAGA HP laser from Thales company. The LSP parameters are listed in Supplementary Section S1. The LSP treatment introduces a compressive stress state in the x-y plane, in the near top surface region of the sample. The same treatment was done on both red-gold and bronze samples.

In order to check for the presence of the ordered phase in the as-built red-gold samples after printing, synchrotron X-ray diffraction experiments were performed at the Materials Science beamline of the Swiss Light Source [19]. The experiments are performed in reflection mode with an 11.5 keV X-ray beam, focused to a size of 0.3 × 0.3 mm (For more information please check Supplementary Section S2).

For the final microscopic observations, the red-gold samples are cut in half along the building direction. The cross section surface is then manually grinded, polished down to 1 µm and finally elec-

tropolished in a solution given in [20], during 20 s at 27 V. The EBSD maps are acquired across the surface of the sample with a Gemini 450 (Zeiss) field emission gun scanning electron microscope, operating at 30 kV. The acquisition is performed with a Symmetry camera and the Aztec acquisition software (Oxford Instruments). The step size is chosen around 1 µm in order to scan a zone large enough to quantify variant selection in a reasonable amount of time. The inverse pole figures have been calculated on subsets at the top parts of the EBSD maps where the grains have a columnar structure.

After printing, the as–built red-gold sample 1 was heat-treated at 250 °C for 3 h, in order to induce the phase transformation. X-ray diffraction and hardness analyses confirm that the as-built sample is almost 100% f.c.c just after printing, and it is almost fully transformed to the f.c.t phase after the hardening heat treatment (see Supplementary Section S3). It is known that as-built L-PBF samples display tensile stress on the top surface and compressive ones in the region below [6,21,22]. Hole drilling measurements performed on the bronze samples (Supplementary Section S4) confirm that the stress in the x-y plane is indeed tensile on top of the sample, with the chosen scanning strategy.

A large EBSD map measured on the x-z cross section of the sample is shown in Fig. 1, according to the scheme of Fig. 1a. Fig. 1-b indicates the inverse pole figure IPZz calculated on top half part of the map of the f.c.t. domains represented in the IPFx and y maps in Fig. 1-c and 1-d, respectively. The top half of the sample is mainly blue and green and the very bottom shows some red domains. The blue and green domains correspond to the variants that have their extension axes in the x-y plane (extension variants), while the red domains have their contraction axis in the x-y plane (contraction variants). Most of the variants have their contraction axis perpendicular to the x-y plane, i.e. their c-axis tends to be along the building direction z. The axial f.c.t. texture intensity given by the multiple of uniform density (MUD) in Fig. 1-b is high (MUD = 30). Such a strong texture of the f.c.t. grains is possible because of the strong axial texture of the parent f.c.c. grains formed during L-PBF. Fig. 1-e shows the f.c.c. parent grains reconstructed from the EBSD data with the Mtex toolbox from Matlab according to a simple method explained in Ref. [24]. Fig. 1-e show a strong initial texture with all grains in reddish color, which means that {001}f.c.c planes are perpendicular to the building discretion z. This initial parent texture is taken into account in the calculation of the degree of variant selection.

In order to quantitatively analyze the variant selection, the Matlab routine detailed in [23] is adapted to a biaxial stress distribution. The variant selection analysis is based on the calculation of the mechanical work of formation of one variant W. This work is expressed as the Frobenius product of $\sigma$, the macroscopic stress tensor, by $\varepsilon^l$, the lattice strain tensor, i.e. $W = \sigma : \varepsilon^l$.
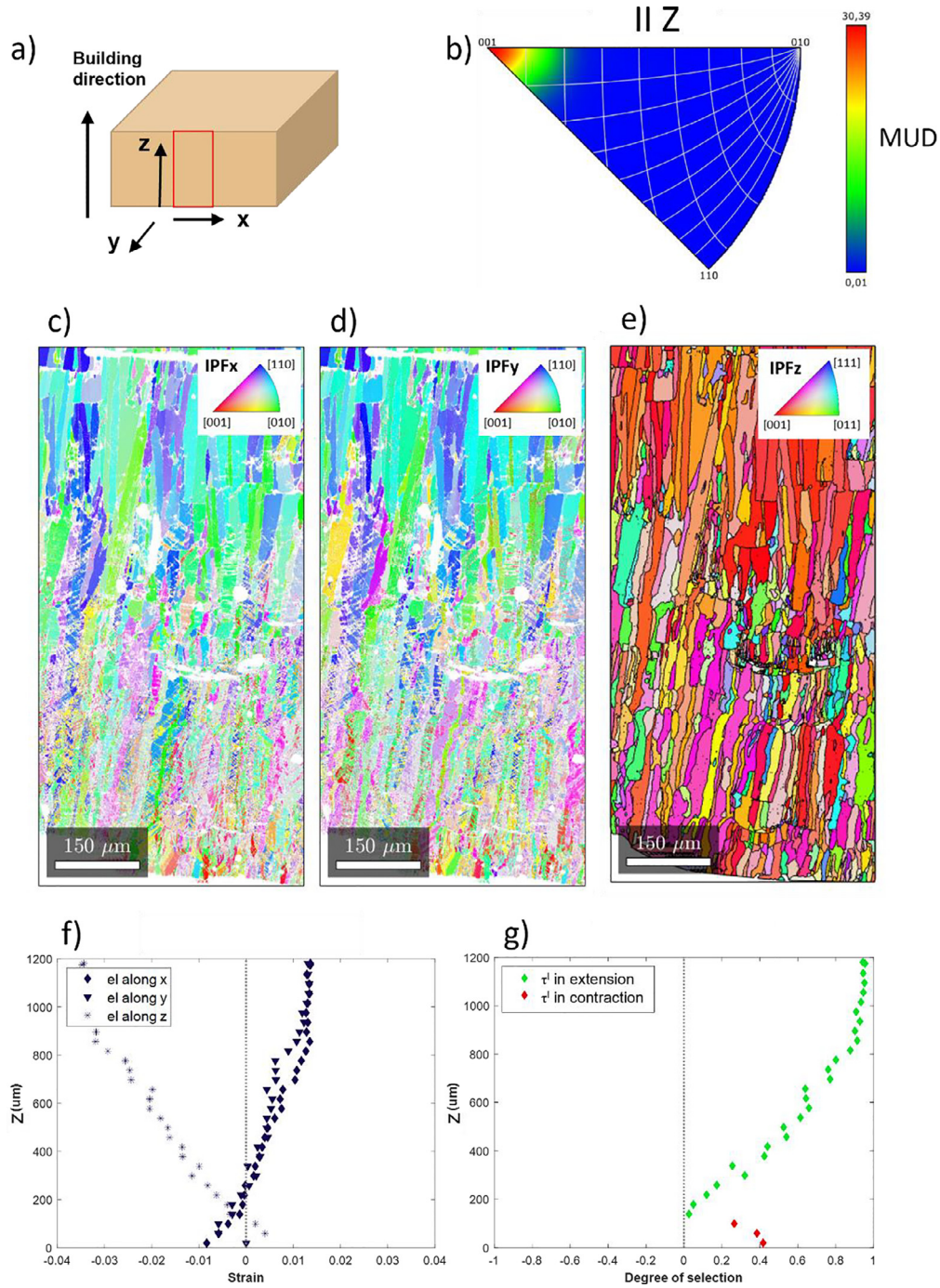
**Fig. 1.** (a) Schematic representation of the samples and location of the EBSD map and (b) Inverse pole figure of the f.c.t. domains of the EBSD map of sample 1 represented in (c) IPFx and (d) IPFy color codes. The x-direction is horizontal, the z (building) direction is vertical, and the y-direction is perpendicular to the page. (e) Reconstructed parent f.c.c. grains in IPFz color code. (f) Evolution of the average lattice strain along the three sample directions with the depth z (0 is the bottom and 1200 μm is the top of the sample) and (g) corresponding degree of variant selection (For interpretation of the references to color in this figure, the reader is referred to the web version of this article.).

The crosshatch L-PBF scanning strategy results in an approximately symmetric residual stress distribution along x and y (see Supplementary Section S4). In addition, the profile of average lattice strain $\bar{\varepsilon}^l$ (Fig. 1-f) is very similar in the x and y directions, which indicates a symmetric distribution of the variant selection in the x and y directions. This is consistent with the symmetric residual stresses.

For the above reasons, we make the assumption that the stress state is equibiaxial, as expressed by the relation (1). In addition, shear stresses and the normal stress in the z-direction are set to 0

since they would have no impact on the analysis.

$$\sigma = \begin{pmatrix} \sigma_x & 0 & 0 \\ 0 & \sigma_x & 0 \\ 0 & 0 & 0 \end{pmatrix} \tag{1}$$

The mechanical work associated to the transformation can then be expressed as $W = \sigma_x(\bar{\varepsilon}_x^l + \bar{\varepsilon}_y^l)$. The degree of variant selection ($\tau$) is the average work deviation from the equi-repartition (Eq. (2)). Thus, $\tau$ is 0 when all the variants are present with the same proportion and 1 if only the maximal work variant is formed
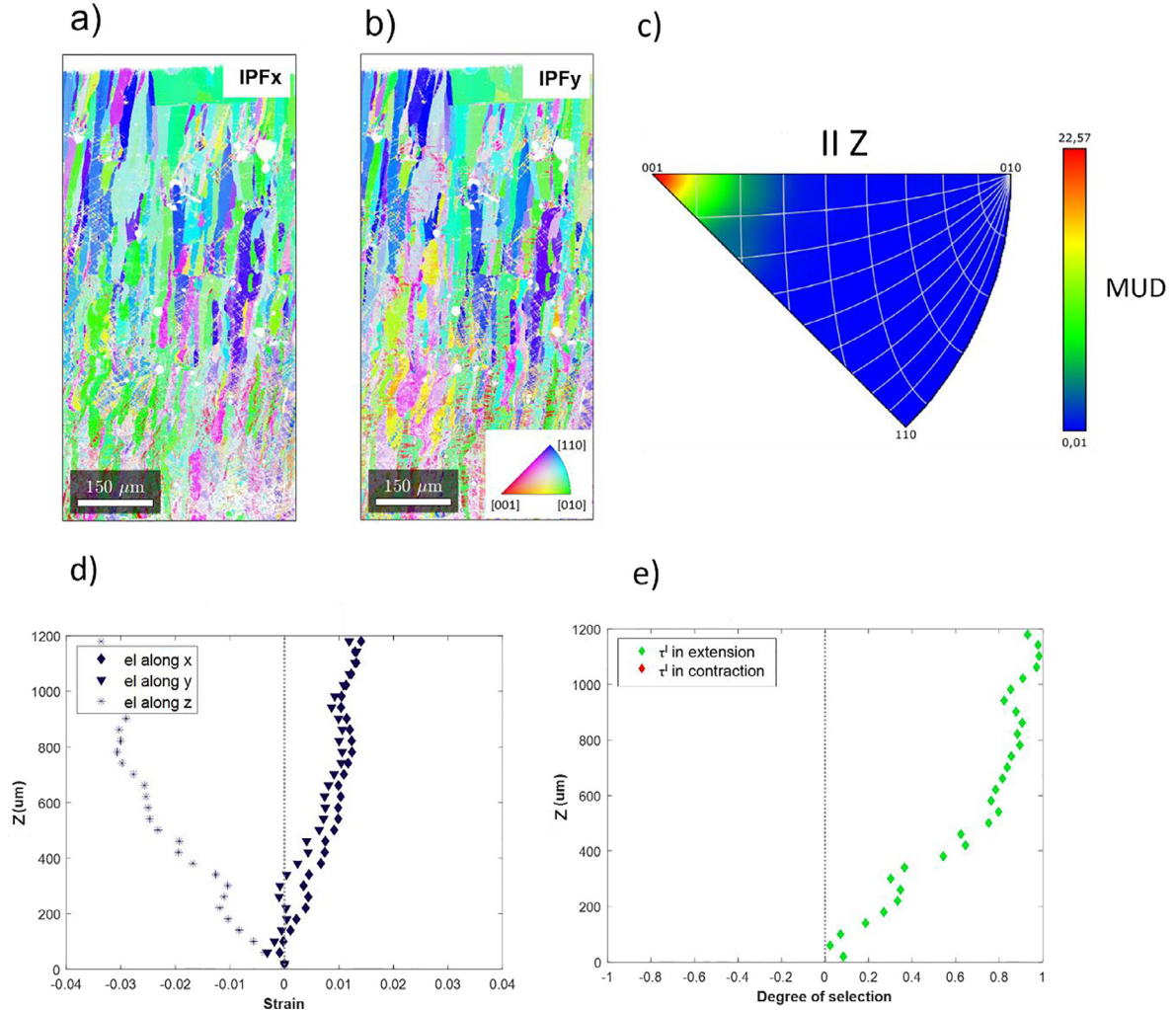
**Fig. 2.** EBSD map of sample 2 after ordering heat treatment with the f.c.t. domains in (a) IPFx coloring and (b) IPFy coloring. The x-direction is horizontal, the z (building) direction is vertical, and the y-direction is perpendicular to the page. (c) Inverse pole figure IPFz of the EBSD map along z direction. (d) Evolution of the average lattice strain along z for three sample directions and (e) corresponding degree of variant selection.

within each grain [23]. The average work value $\bar{W}$ is compared to the hypothetical equi-repartition of the three variants within each grain ($\bar{W}_{equi}$), and also to the case where only the maximal work variant is present in each grain ($\bar{W}_{max}$). It can be simplified and expressed in terms of lattice strains in Eq. (2).

$$\tau = \frac{\bar{W} - \bar{W}_{equi}}{\bar{W}_{max} - \bar{W}_{equi}} = \frac{\left(\bar{\varepsilon}_x^l + \bar{\varepsilon}_y^l\right) - \left(\bar{\varepsilon}_x^l + \bar{\varepsilon}_y^l\right)_{equi}}{\left(\bar{\varepsilon}_x^l + \bar{\varepsilon}_y^l\right)_{max} - \left(\bar{\varepsilon}_x^l + \bar{\varepsilon}_y^l\right)_{equi}} \quad (2)$$

Fig. 1-g shows the evolution of the degree of variant selection $\tau$ across the thickness of sample 1. It confirms that extension variants are selected on top of the sample. In addition, a small compressive lattice strain is observed close to the bottom of the sample. The variant selection on top of the sample is almost maximal (close to 1), which has not been observed so far in conventional samples [13,23]. In addition, the average lattice strain on the top surface is very close to the one derived from the change of the crystallographic unit cell, i.e. 1.5% in extension and −3.9% in compression. This result is explained by the strong initial texture of the sample. For comparison, the strain in a non-textured polycrystal was computed in [13] as 1.12% in extension and −2.24% in contraction.

In order to study the influence of a compressive stress on the final texture, the LSP treatment is performed on another as-built red-gold sample 2, in its f.c.c. phase. The LSP treatment induces compressive stress in the region near the top surface [3]. Sample 2 is then heat-treated at 250 °C for 3 h, to induce the phase transformation. It is expected that the compressive stress near the top surface leads to variant selection with the contraction axis of the f.c.t. lattice in the x-y plane (contraction variants).

The EBSD map of the cross section of sample 2 is presented in Fig. 2. Fig. 2a–c, show the same texture as in sample 1. This result is confirmed by the evolution of the degree of variant selection with z, given in Fig. 2-d, again similar to that of sample 1 (Fig. 1). This distribution of variant selection is not consistent with the LSP induced compressive stress in the sample before the phase transformation. Yet, the presence of high compressive stresses on the top part of the sample has been confirmed by hold drilling measurements on the equivalent bronze sample (Supplementary Section S4).

As a comparison, another red-gold sample 3 has been heat treated at 600 °C for 45 min after printing, in order to re-initialize the thermo-mechanical history of the material [26]. The sample is then water quenched to prevent the f.c.c. → f.c.t. transformation. Similarly to sample 2, the LSP treatment is conducted to introduce compressive stresses near the top surface of the sample, and this operation is followed by a heat treatment at 250 °C for 3 h to induce the phase transformation. This time, and unlike sample 2, the
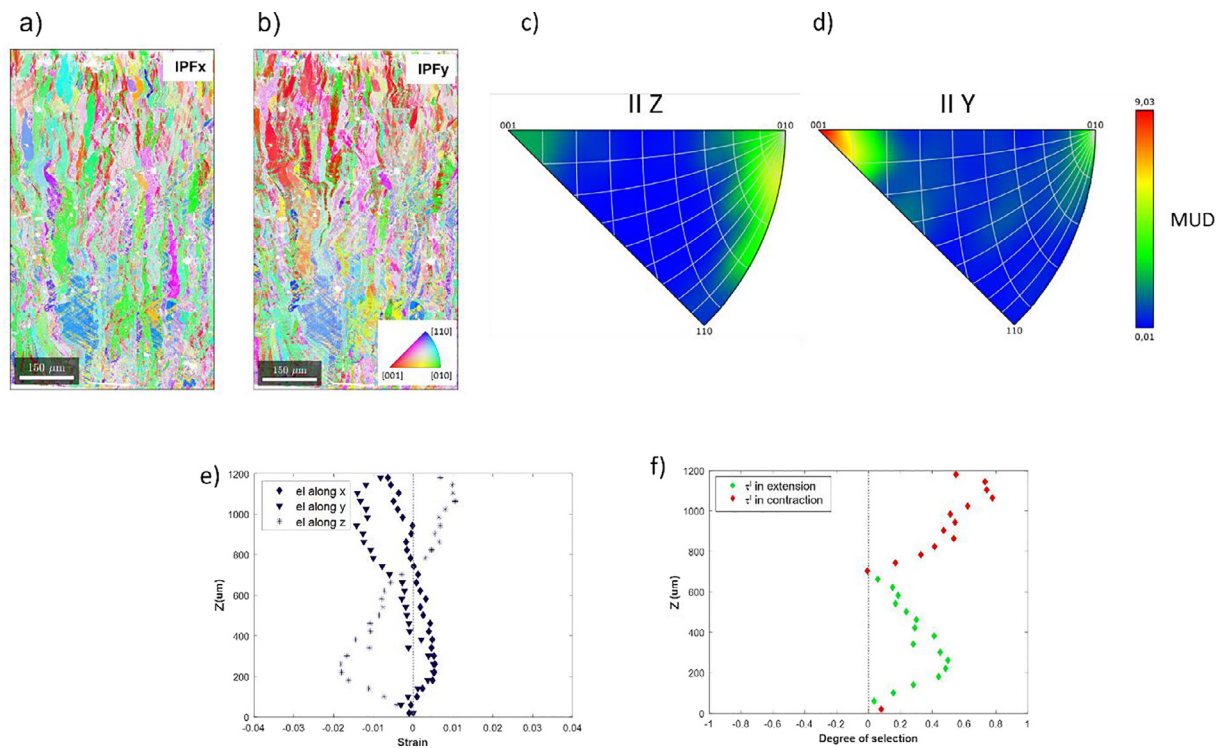
**Fig. 3.** EBSD map of sample 3 after ordering heat treatment with the f.c.t. domains in (a) IPFx coloring and (b) IPFy coloring. The x-direction is horizontal, the z (building) direction is vertical, and the y-direction is perpendicular to the page. (c) and (d) indicate the inverse pole figure of the EBSD map along z and y, respectively. (e) Evolution with z of the average lattice strain along the three sample directions and (f) corresponding degree of variant selection.
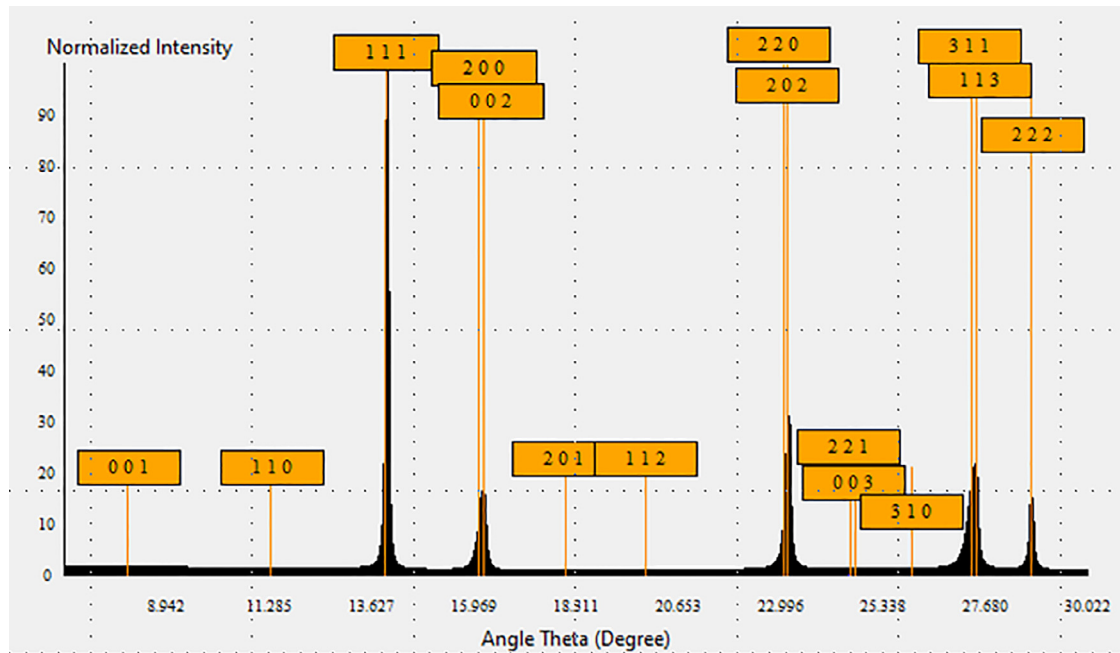


**Fig. 4.** X-ray diffractogram of the as-built red-gold sample with the main peaks labelled with a L10 tetragonal phase.

texture in sample 3 is consistent with the presence of compressive stresses on top of the sample (Fig. 3). The red IPFx and IPFy coloring of the f.c.t. variants in Fig. 3-a and b indicates the presence of contraction variants on top of the sample. The inverse pole figures IPFz and IPFy of the EBSD map (Fig. 3-c,d) confirm the change in variant selection from axial texture (c//z in sample 1 and 2) to radial texture (c in the x-y plane in sample 3). The texture density (MUD = 9) is lower than in sample 1 and 2 mainly because

of this change of the axial to radial texture. The lattice distortion evolution with z plotted in Fig. 3-e confirms a contraction along the x and y directions, and an extension along the z direction near the top surface. The lattice distortion is slightly different in the x and y directions, but the tendency is similar. The variant selection as a function of z confirms the over-representation of contraction variants in the top half of the sample and extension variants in the bottom part (Fig. 3-f). This profile is in good agreement
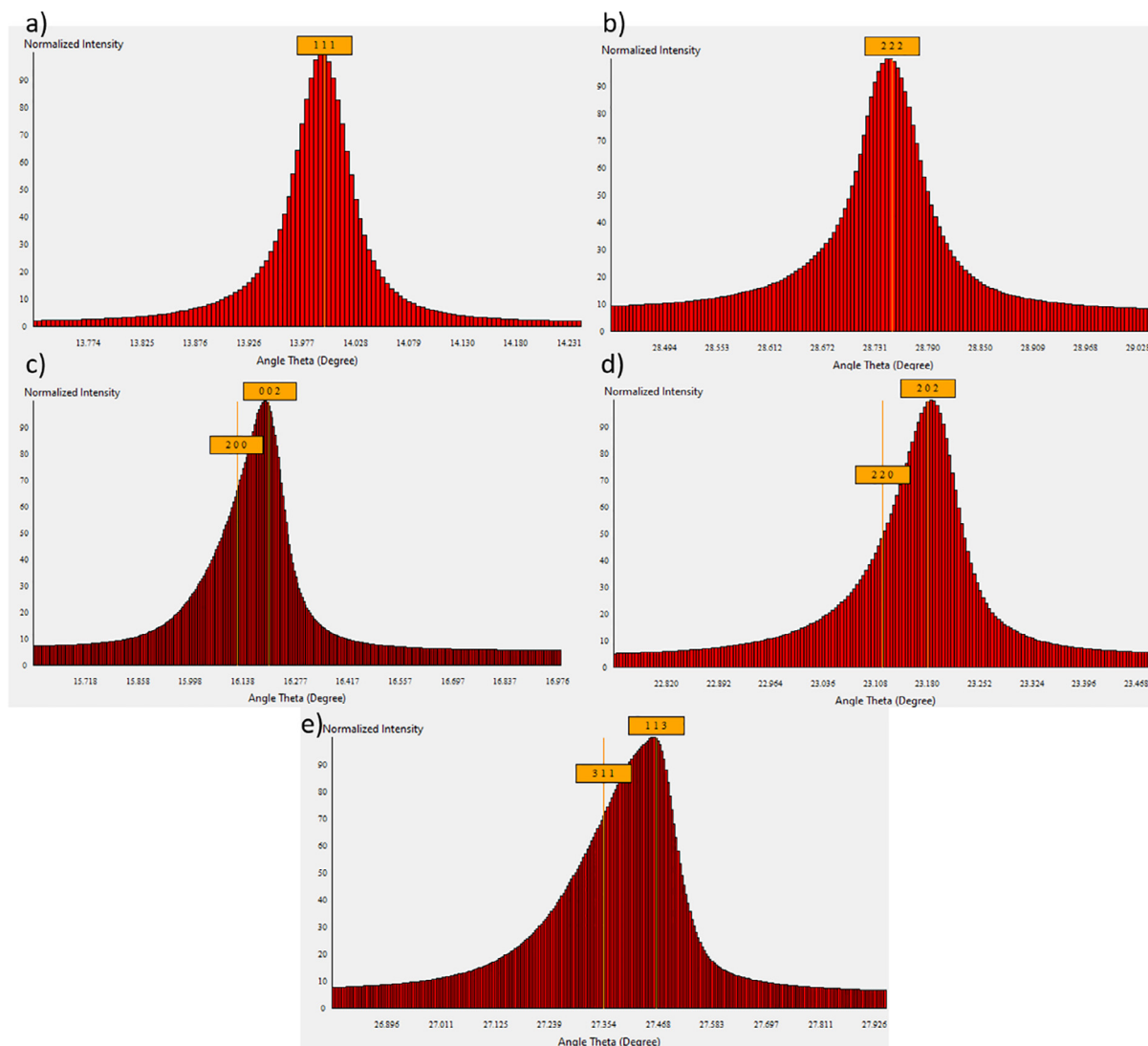
**Fig. 5.** Tetragonality of the L1$_0$ phase deduced from the peak shapes. (a, b) The peak are symmetric only for {111} and {222}, and (c, d, e) asymmetric for the other peaks.

with the expected stress profile induced by the LSP treatment [3].

The discrepancy between the textures of sample 2 and sample 3 is of interest as the two samples have undergone the same LSP and hardening treatments. The only difference between the two samples is the intermediate heat treatment at 600 °C, before LSP. The variant selection profile in sample 3 indicates that the LSP treatment has the expected effect on the material. The compressive stress on top of the sample (confirmed by the hole drilling measurements) induced contraction variant selection. The fact there is no effect of the LSP treatment on sample 2 demonstrates a mechanism preventing the expected variant selection. This effect is removed by the intermediate annealing at 600 °C.

Although normal lab-XRD measurements show no presence of the f.c.t. phase after printing (Supplementary Section S3, as-built sample), small nuclei of ordered f.c.t. phase are likely to be formed due to the non-negligible heating of the samples during L-PBF processing. Finite element simulations confirm that the temperature increases sufficiently high for the ordering phase transformation to take place during the deposition of new layers [16,26] (see also Supplementary Section S5). The presence of a non-negligible amount of tetragonal phase was confirmed by Synchrotron X-ray diffraction. The full diffractogram is shown in Fig. 4. The peaks could be satisfactorily simulated by a L1$_0$ tetragonal phase with lattice parameters close to a ~ 3.87 Å and c ~ 3.85 Å (c/a ~ 0.995).

The c/a ratio of the L1$_0$ phase was deduced from the broadening and asymmetry of the peaks observed for all the reflections except {111} and their multiple, as shown in Fig. 5. The c/a value is approximate, but cannot be lower than 0.990.

The strong asymmetry of the peaks in Fig. 5 c,d,e also shows that the density of the tetragonal phase is significant. However, this tetragonal phase is not fully ordered. If it were the case, some extra reflections with Miller $h$, $k$, $l$ indices that are null for the cubic phase should be visible, such as (001), (110), (210), (201), (102), (211), (112). Some of them are labelled in Fig. 4. However, their intensity is very low, and only broad bumps are visible for some frequencies between the (200) and (220) peaks (see Supplementary Section S6). This is explained by the low degree of ordering of the L1$_0$ phase. Different tetragonal phases were created with various degrees of occupancy of the Cu and Au atoms in the two types of sites of the L1$_0$ structure (noted A for Cu sites and B for Au sites), and the intensity of the extra reflections were compared with the experiments. We determined that the degree of order cannot exceed 10%, meaning that the Cu atoms have 10% more probability to occupy A sites than B sites.

The very high density of partially ordered $L1_0$ phase with a c/a ratio very close to 1 confirms that the cubic to tetragonal transformation is spatially quite homogeneous. As the transformation proceeds, the average degree of ordering increases, while the average c/a ratio decreases [29–31]. The spatial homogeneity of the transformation can explain the origin of TADA effect [13]. The variant selection is determined by the stress state at the very beginning of the phase transformation. When the stress is removed after these early stages, the variant selection keeps proceeding the same way, as the phase transformation continues. In a companion paper [14], it is proved that the persistence of the variant selection can even occur under opposite loading. The phenomenon of persistence of variant selection is at the origin of the surprising absence of LSP treatment effect on the variant selection and final texture in sample 2.

In conclusion, variant selection along the cross section of additively manufactured red-gold samples has been quantified by EBSD, using the maximal work criterion. Despite the change of stress state induced by a LSP treatment before the hardening heat treatment, the variant selection in sample 2 and the as-built L-PBF sample 1 is the same. This result is explained by the persistence of variant selection, whereby the formation of small f.c.t. domains in the printed sample occurs in the near surface region under tensile stress conditions. The extension variant selection initiated during L-PBF does not change and the f.c.t. domains will continue to grow accordingly, even if the stress state is subsequently changed by LSP. This has been confirmed by conducting an intermediate heat treatment at 600 °C before LSP to remove the primary ordered domains formed during the manufacturing process. As a result, after LSP and heat treatment, the variant selection profile in sample 3 matches the profile expected by the compressive stress induced by LSP.

## Declaration of Competing Interest

The authors declare that they have no known competing financial interests or personal relationships that could influence the work and results reported in this paper.

## Acknowledgments

## Supplementary materials

Supplementary material associated with this article can be found, in the online version, at doi:10.1016/j.scriptamat.2021.114490.

## References

[1] L.G. Hector, R.B. Hetnarski, R.B. Hetnarski, in: Mechanics and Mathematical Methods–Series of Handbooks, North-Holland, Amsterdam, 1996, pp. 453–531.
[2] B. Vranchen, Study of Residual Stresses in Selective Laser Melting, KU Leuven, 2016.
[3] N. Kalentics, E. Boillat, P. Peyre, S. Ćirić-Kostić, N. Bogojević, R.E. Logé, Addit. Manuf. 16 (2017) 90–97.
[4] N. Kalentics, A. Burn, M. Cloots, R.E. Logé, Int. J. Adv. Manuf. Technol. 101 (2019) 1247–1254.
[5] N. Kalentics, N. Sohrabi, H.G. Tabasi, S. Griffiths, J. Jhabvala, C. Leinenbach, A. Burn, R.E. Logé, Addit. Manuf. 30 (2019) 100881.
[6] N. Kalentics, M.O.V. de Seijas, S. Griffiths, C. Leinenbach, R.E. Logé, Addit. Manuf. 33 (2020) 101112.
[7] H. Okamoto, D.J. Chakrabarti, D.E. Laughlin, T.B. Massalski, J. Phase Equilib. 8 (1987) 454–474.
[8] G.C. Kuczynski, R.F. Hochman, M. Doyama, J. Appl. Phys. 26 (1955) 871–878.
[9] M. Garcia-Gonzalez, S. Van Petegem, N. Baluc, S. Hocine, M. Dupraz, F. Lalire, H. Van Swygenhoven, Scr. Mater. 170 (2019) 129–133.
[10] A.Y. Volkov, V.A. Kazantsev, Phys. Metals Metallogr. 113 (2012) 62–71.
[11] M. Ohta, T. Shiraishi, R. Ouchida, M. Nakagawa, S. Matsuya, J. Alloy. Compd. 265 (1998) 240–248.
[12] S. Kohara, G.C. Kuczynski, Acta Metall. 4 (1956) 221–222.
[13] M.N.D. Larcher, C. Cayron, A. Blatter, R. Soulignac, R.E. Logé, Acta Mater. 198 (2020) 242–256.
[14] M.N.D. Larcher, C. Cayron, A. Blatter, R. Soulignac, R.E. Logé, Journal of Alloys and Compounds 899 (2022) 163364.
[15] J. Jhabvala, Study of the Consolidation Process under Macro- and Microscopic Thermal Effects in Selective Laser Sintering and Selective Laser Melting, EPFL PP, Lausanne, 2010.
[16] H. Ghasemi-Tabasi, J. Jhabvala, E. Boillat, T. Ivas, R. Drissi-Daoudi, R.E. Logé, Addit. Manuf. 36 (2020) 101496.
[17] H. Ghasemi-Tabasi, P. Trtik, J. Jhabvala, M. Meyer, C. Carminati, M. Strobl, R.E. Logé, Appl. Sci. 11 (2021) 1512, doi:10.3390/app11041512.
[18] H. Ghasemi Tabasi, Understanding Thermomechanical Treatments Induced by Laser Powder Bed Fusion Process, EPFL, 2021.
[19] P.R. Willmott, D. Meister, S.J. Leake, M. Lange, A. Bergamaschi, M. Boge, M. Calvi, C. Cancellieri, N. Casati, A. Cervellino, Q. Chen, C. David, U. Flechsig, F. Gozzo, B. Henrich, S. Jaggi-Spielmann, B. Jakob, I. Kalichava, P. Karvinen, J. Krempasky, A. Ludeke, R. Luscher, S. Maag, C. Quitmann, M.L. Reinle-Schmitt, T. Schmidt, B. Schmitt, A. Streun, I. Vartiainen, M. Vitins, X. Wang, R. Wullschleger, J. Synchrotron Radiat. 20 (2013) 667–682.
[20] R. Wolf, Micron 8 (1977) 171–172.
[21] J.L. Bartlett, X. Li, Addit. Manuf. 27 (2019) 131–149.
[22] Y. Liu, Y. Yang, D. Wang, Int. J. Adv. Manuf. Technol. 87 (2016) 647–656.
[23] M.N.D. Larcher, C. Cayron, A. Blatter, R. Soulignac, R.E. Loge, J. Appl. Crystallogr. 52 (2019) 1202–1213.
[24] F. Bachmann, R. Hielscher, H. Schaeben, Solid State Phenom. 160 (2010) 63–68.
[25] M. Garcia-Gonzalez, S. Van Petegem, N. Baluc, M. Dupraz, V. Honkimaki, F. Lalire, H. Van Swygenhoven, Acta Mater. 191 (2020) 186–197.
[26] S. Hocine, H. Van Swygenhoven, S. Van Petegem, Addit. Manuf. 37 (2021) 101747.
[27] G. Borelius, J. Inst. Metals 74 (1948) 17–31.
[28] J.L. O'Brien, G.C. Kuczynski, Acta Metall. 7 (1959) 803–806.
[29] Y. Tanaka, K. Udoh, K. Hisatsune, K. Yasuda, Mater. Trans. JIM 39 (1998) 87–94.